J. Fluid Mech. (2019), *vol.* 875, *pp.* 101–123.
doi:10.1017/jfm.2019.499

Decomposition of the mean skin-friction drag in compressible turbulent channel flows

Weipeng Li[1,2,†], Yitong Fan[1], Davide Modesti[3] and Cheng Cheng[1]

[1]School of Aeronautics and Astronautics, Shanghai Jiao Tong University, Shanghai, 200240, China

[2]Engineering Research Center of Gas Turbine and Civil Aero Engine, Ministry of Education, China

[3]Department of Mechanical Engineering, The University of Melbourne, Victoria 3010, Australia

(Received 19 December 2018; revised 13 June 2019; accepted 17 June 2019;
first published online 18 July 2019)

The mean skin-friction drag in a wall-bounded turbulent flow can be decomposed into different physics-informed contributions based on the mean and statistical turbulence quantities across the wall layer. Following Renard & Deck's study (*J. Fluid Mech.*, vol. 790, 2016, pp. 339–367) on the skin-friction drag decomposition of incompressible wall-bounded turbulence, we extend their method to a compressible form and use it to investigate the effect of density and viscosity variations on skin-friction drag generation, using direct numerical simulation data of compressible turbulent channel flows. We use this novel decomposition to study the skin-friction contributions associated with the molecular viscous dissipation and the turbulent kinetic energy production and we investigate their dependence on Reynolds and Mach number. We show that, upon application of the compressibility transformation of Trettel & Larsson (*Phys. Fluids*, vol. 28, 2016, 026102), the skin-friction drag contributions can be only partially transformed into the equivalent incompressible ones, as additional terms appear representing deviations from the incompressible counterpart. Nevertheless, these additional contributions are found to be negligible at sufficiently large equivalent Reynolds number and low Mach number. Moreover, we derive an exact relationship between the wall heat flux coefficient and the skin-friction drag coefficient, which allows us to relate the wall heat flux to the skin-friction generation process.

Key words: high-speed flow, compressible boundary layers

1. Introduction

In a wall-bounded turbulent flow, the mean skin-friction drag has been identified to be much higher than that in a laminar case at the same Reynolds number. It contributes to the total drag up to 50 % for commercial aircraft, 90 % for submarines and almost 100 % for long pipe and channel flows (Gad-el Hak 1994). Understanding the mean skin-friction drag generation and its associated near-wall dynamical system is of fundamental and practical importance, particularly for the evaluation of aerodynamic/hydrodynamic performance and design of drag reduction approaches.

† Email address for correspondence: liweipeng@sjtu.edu.cn

Although the mean skin-friction drag is a wall property, as can be directly calculated from the normal gradient of the mean streamwise velocity at the wall, it is connected to the mean and statistical turbulence quantities across the wall layer and can be further decomposed into various physics-informed components according to different mathematical derivations and physical interpretations. Fukagata, Iwamoto & Kasagi (2002) derived a simple relationship (also referred to as the FIK identity) between the skin-friction coefficient and the Reynolds shear stress distribution for three canonical wall-bounded turbulent flows, with three successive integrations of the mean momentum balance equation. For instance, in a smooth incompressible turbulent channel flow the relation can be cast as

$$C_f = \underbrace{\frac{6}{Re_b}}_{C_{f1,FIK}} + \underbrace{\frac{6}{u_b^2}\int_0^h \left(1-\frac{y}{h}\right)\left(-\langle u'v'\rangle\right)\frac{\mathrm{d}y}{h}}_{C_{f2,FIK}}, \tag{1.1}$$

where $Re_b = hu_b/\nu$ is the bulk Reynolds number (with h being the channel half-height, u_b the bulk velocity, ν the kinematic viscosity), y is the distance from the wall surface and $-\langle u'v'\rangle$ is the Reynolds shear stress. Equation (1.1) provides a decomposition of the skin-friction coefficient into a 'laminar' ($C_{f1,FIK}$) and a 'turbulent' ($C_{f2,FIK}$) contribution, allowing us to quantify the effect of the relative amount of skin-friction drag directly associated with the Reynolds stress. Several modifications to the FIK identity have been proposed in the literature. For instance, Peet & Sagaut (2009) and Bannier, Garnier & Sagaut (2015) extended the FIK identity to complex geometries, to investigate the skin-friction drag reduction with riblets. Modesti *et al.* (2018) generalized the FIK identity to arbitrarily complex geometries by interpreting the mean momentum balance equation as a Poisson equation for the mean velocity and using it to study the skin-friction drag generation in square duct flows. For flat-plate boundary layers, Mehdi & White (2011) modified the FIK identity by replacing the explicit streamwise gradients with the wall-normal gradient of the total stress on the basis of the Navier–Stokes equation, in order to avoid experimental measurements of streamwise gradients affected by large uncertainties. Moreover, to overcome the difficulty in measuring complete statistics across the whole boundary layer, Mehdi *et al.* (2014) proposed another modified FIK identity in which the upper integration bound may end at any arbitrary location within the boundary layer. Over the years, the FIK identity has been widely used in numerous studies: Iwamoto *et al.* (2005), Deck *et al.* (2014), Kametani *et al.* (2015), de Giovanetti, Hwang & Choi (2016), to name a few.

Despite the additional insights provided by (1.1), the FIK identity can be difficult to physically interpret (Renard & Deck 2016). One of the key controversial issues is that there is no simple interpretation for the three successive integrations and no physics-informed explanation for the linearly weighted Reynolds shear stress. An alternative and more objective skin-friction drag decomposition method was proposed by Renard & Deck (2016), referred to as the RD identity hereafter. The RD identity was derived from the mean streamwise kinetic-energy equation in an absolute reference frame in which the undisturbed fluid is not moving. It characterizes the power of skin-friction drag as an energy transfer from the wall to the fluid by means of dissipation of molecular viscosity and turbulent kinetic energy (TKE) production. The authors showed that this method overcomes some of the drawbacks of the FIK identity, allowing an improved physical interpretation of the skin-friction drag

generation mechanism. In the case of turbulent channel flow the RD identity can be written as

$$C_f = \underbrace{\frac{2}{u_b^3}\int_0^h \nu\left(\frac{\partial\langle u\rangle}{\partial y}\right)^2 \mathrm{d}y}_{C_{f1,RD}} + \underbrace{\frac{2}{u_b^3}\int_0^h (-\langle u'v'\rangle)\frac{\partial\langle u\rangle}{\partial y}\,\mathrm{d}y}_{C_{f2,RD}}, \tag{1.2}$$

where $\langle u\rangle$ is the mean streamwise velocity, $C_{f1,RD}$ represents the contribution from direct molecular viscous dissipation and $C_{f2,RD}$ characterizes the contribution associated with the production of TKE. Renard & Deck (2016) further analysed the Reynolds number dependence of the decomposed terms, and shed light on the importance of logarithmic-layer dynamics in the skin-friction drag generation.

Yoon *et al.* (2016) related the mean skin-friction drag to the motions of vortical structures by integrating the mean vorticity transport equation, and identified contributions from advective vorticity transport, vortex stretching, viscosity and heterogeneity. Hwang & Sung (2017) employed this method to examine the significant contributions associated with large-scale turbulent motions. Kim *et al.* (2017) used this method to evaluate the influence of a large-eddy breakup device on the near-wall turbulence and skin-friction drag reduction.

These mean skin-friction drag decomposition methods have all been developed for incompressible flows, whereas only few studies can be found for compressible wall-bounded turbulence. Gomez, Flutet & Sagaut (2009) generalized the FIK identity to compressible flows and studied the compressibility effects on the mean skin-friction drag generation, but they actually have not fully clarified the effect of compressibility on the different contributions. In particular, in their study only the components associated with viscosity variations are ascribed to compressible effects, but compressibility also remarkably impacts the density and therefore these contributions from density variations should be marked as 'compressible' contributions as well. One objective of this study is to extend the physics-informed RD identity into a compressible form and use it to evaluate compressibility effects more precisely.

As for the compressibility effects, they can be classified into two kinds: (i) indirect effects due to the variation of the thermodynamic properties, such as density and viscosity; (ii) genuine effects caused by dilatational velocity fluctuations and thermodynamic fluctuations. Based on the Morkovin hypothesis (Morkovin 1962), the latter could be neglected for non-hypersonic boundary layers (say, Mach number $M < 5$), since the local root mean square (r.m.s.) fluctuating Mach number is negligible. The effect of density and viscosity variations in wall-bounded turbulence can be accounted for by using appropriate transformations of the mean streamwise velocity and Reynolds stresses, allowing us to collapse the compressible flow statistics onto the 'universal' incompressible distributions. A classical transformation of the mean streamwise velocity and Reynolds shear stress has been developed by van Driest (1951) using inner-layer similarity arguments. This transformation is rather accurate in the case of adiabatic walls but fails on isothermal walls (Huang & Coleman 1994), especially for cases with strong heat transfer. Huang, Coleman & Bradshaw (1995) proposed a semi-local scaling for transforming the turbulent stresses which yields better collapse onto the corresponding incompressible distributions in a wide Mach number range, 0.3–3.5 (Foysi, Sarkar & Friedrich 2004). Patel *et al.* (2015), Trettel & Larsson (2016) showed that the semi-local Reynolds number is the appropriate equivalent Reynolds number to compare flows across Mach numbers. Moreover, Patel, Boersma & Pecnik (2016) showed that near-wall streaks are less coherent in the

cases where the semi-local Reynolds number increases away from the wall. Pecnik & Patel (2017) also applied the semi-local scaling for deriving transformed conservation equation of the turbulent kinetic energy, which shows that the 'leading-order effect' of variable density and viscosity on turbulence in wall-bounded flows can effectively be characterized by the semi-local Reynolds number. Recently, Trettel & Larsson (2016) proposed another transformation based on the logarithmic-layer scaling and near-wall momentum conservation which shows satisfactory agreements with incompressible flow data in a wide range of Reynolds and Mach numbers (Modesti & Pirozzoli 2016). The good accuracy of Trettel & Larsson (2016) transformation suggests that it can be used to scale the decomposed skin-friction constituents, to obtain 'universal' distributions that match the incompressible ones.

In addition to the skin-friction drag, wall heat transfer is another subject of concern in this paper. Wall heat transfer can be directly linked to the skin-friction drag using temperature–velocity correlations, such as the one proposed by Walz (1959). Direct numerical simulation data have shown that Walz's relation is rather accurate on adiabatic walls, whereas large deviations are observed for increasing wall heat transfer (Duan, Beekman & Martin 2010, 2011; Zhang *et al.* 2014). Zhang *et al.* (2014) replaced the recovery factor in Walz's equation and generalized it for non-adiabatic flows. Although these correlations give an analogy between the temperature and velocity, they are derived empirically under specific conditions or assumptions. Regarding incompressible boundary layers, Ebadi, Mehdi & White (2015) proposed an integral formula of wall heat flux, which ascribes the wall heat flux to contributions related to mean temperature profile, turbulent heat flux and gradient of total (molecular and turbulent) heat flux. In the present study, we will provide an exact correlation between the wall heat flux and skin-friction drag coefficient, from the energy conservation equation of compressible turbulent channel flows, giving the relationship between momentum transport and heat transfer at the wall.

This paper is organized in the following way. A compressible counterpart of the RD identity (1.2) for the skin-friction coefficient is derived in § 2, as well as the formulation for the wall heat flux. Direct numerical simulations of five supersonic turbulent channel cases are described in § 3. In § 4, contributions of the molecular viscous dissipation and the TKE production are quantified. We investigate the Reynolds number and Mach number dependence of the mean skin-friction drag generation via the assessment of the turbulence quantities across the channel. In order to obtain universal distributions such as those in incompressible channel flows and capture the 'compressible' contributions caused by the density and viscosity variations, compressibility transformations are employed to scale the decomposed constituents. Finally, concluding remarks are given in § 5.

2. Decomposition of the mean skin-friction drag and wall heat flux in compressible turbulent channel flows

Firstly, the RD identity is generalized into a compressible form for compressible turbulent channel flows, and the physical interpretations of each component are discussed. For flat-plate boundary layers, the compressible RD identity is given in appendix A. Secondly, we derive an exact correlation between the wall heat flux coefficient and the skin-friction drag coefficient.

2.1. *Mean skin-friction drag decomposition*

The mean skin-friction drag coefficient C_f can be cast as

$$C_f = \frac{2\tau_w}{\rho_b u_b^2} = \frac{2}{Re_b}\frac{\partial(\langle u\rangle/u_b)}{\partial(y/h)}|_{wall}, \tag{2.1}$$

where $\langle\cdot\rangle$ is the Reynolds averaging operator, τ_w is the wall shear stress, u is the streamwise velocity, y is the wall distance and Re_b is the bulk Reynolds number. In compressible channel flows, Re_b $(=\rho_b u_b h/\mu_w)$ is based on the channel half-height h, bulk density $\rho_b = (1/h)\int_0^h \langle\rho\rangle\,\mathrm{d}y$, bulk velocity $u_b = (1/\rho_b h)\int_0^h \langle\rho u\rangle\,\mathrm{d}y$ and dynamic viscosity at the wall μ_w. Hereafter, x, y and z stand for the streamwise, wall-normal and spanwise directions, respectively.

Considering the channel flow, we assume (i) no-slip condition at the wall surfaces, (ii) statistical homogeneity in the spanwise and streamwise directions and (iii) symmetry with respect to the central plane of the channel. Under these hypotheses the compressible Reynolds-averaged momentum equation in the streamwise (x-) direction is

$$\frac{\partial\langle\rho u\rangle}{\partial t} + \frac{\partial\langle\rho uv\rangle}{\partial y} = \frac{\partial\langle\tau_{yx}\rangle}{\partial y} + \langle\rho f\rangle, \tag{2.2}$$

where u and v are respectively the streamwise and wall-normal components of the transient velocity, ρ is density, t is time and τ_{yx} is the shear stress in the streamwise direction. A uniform body force f is added to drive the flow in the streamwise direction (Huang *et al.* 1995). Integrating (2.2) from the wall surface to the central plane gives

$$\frac{\partial Q}{\partial t} = -\tau_w + \rho_b h f, \tag{2.3}$$

where $Q = \int_0^h \langle\rho u\rangle\,\mathrm{d}y$ is the mass flow rate across the traverse plane. To ensure the flow stability and continuity, $\partial Q/\partial t = 0$ is set up. Then we get

$$f = \frac{\tau_w}{\rho_b h}. \tag{2.4}$$

For an arbitrary variable ϕ, its Favre average $\{\phi\}$ is defined as $\langle\rho\phi\rangle/\langle\rho\rangle$, and the double prime $''$ denotes the turbulent fluctuations with respect to the Favre average, i.e. $\phi'' = \phi - \{\phi\}$. If we rewrite the left-hand side of (2.2) in the form of Favre average, we have

$$\frac{\partial\langle\rho u\rangle}{\partial t} + \frac{\partial\langle\rho uv\rangle}{\partial y} = \{u\}\left(\frac{\partial\langle\rho\rangle}{\partial t} + \frac{\partial\langle\rho v\rangle}{\partial y}\right) + \langle\rho\rangle\left(\frac{\partial\{u\}}{\partial t} + \{v\}\frac{\partial\{u\}}{\partial y}\right) + \frac{\partial\langle\rho\rangle\{u''v''\}}{\partial y}. \tag{2.5}$$

Using the continuity equation and the total derivative $D\{\cdot\}/Dt = \partial\{\cdot\}/\partial t + \{v\}(\partial\{\cdot\}/\partial y)$ and substituting (2.4) and (2.5) into (2.2), we have

$$\langle\rho\rangle\frac{D\{u\}}{Dt} = -\frac{\partial\langle\rho\rangle\{u''v''\}}{\partial y} + \frac{\partial\langle\tau_{yx}\rangle}{\partial y} + \frac{\langle\rho\rangle}{\rho_b h}\tau_w. \tag{2.6}$$

Following the derivation of the original RD identity (Renard & Deck 2016), we transform the initial reference frame (attached to the wall) into an absolute reference frame, where the wall is moving at the speed of $-u_b$. Let the subscript a represent the variables in the absolute frame. Then the time t_a, density ρ_a, coordinates x_a and y_a and velocity u_a and v_a satisfy

$$t_a = t, \quad \rho_a = \rho, \quad x_a = x - u_b t, \quad y_a = y, \quad u_a = u - u_b, \quad v_a = v. \tag{2.7a–f}$$

Substituting (2.7) into (2.6) yields

$$\langle \rho_a \rangle \frac{D\{u_a\}}{Dt_a} = -\frac{\partial \langle \rho_a \rangle \{u_a'' v_a''\}}{\partial y_a} + \frac{\partial \langle \tau_{yx} \rangle}{\partial y_a} + \frac{\langle \rho_a \rangle}{\rho_b h} \tau_w. \tag{2.8}$$

In the absolute reference frame, the averaged streamwise kinetic energy of unit mass $\{K_a\}$ is defined as $\{u_a\}^2/2$. Thus multiplying both sides of (2.8) by $\{u_a\}$, we have the energy budget equation,

$$\langle \rho_a \rangle \frac{D\{K_a\}}{Dt_a} = -\{u_a\} \frac{\partial \langle \rho_a \rangle \{u_a'' v_a''\}}{\partial y_a} + \{u_a\} \frac{\partial \langle \tau_{yx} \rangle}{\partial y_a} + \{u_a\} \frac{\langle \rho_a \rangle}{\rho_b h} \tau_w. \tag{2.9}$$

Moreover, in statistically temporally and spatially homogeneous channel flows, the rate of mean streamwise kinetic energy in the absolute frame, $D\{K_a\}/Dt_a$, is definitely zero for that $\{v\} = 0$.

A single integration over the half-channel is then performed on (2.9), using no-slip boundary conditions at the wall and symmetry boundary conditions at the centreline leads to the formula of the skin-friction coefficient in the absolute reference frame,

$$C_f = \underbrace{\frac{2}{\rho_b u_b^3} \int_0^h \langle \tau_{yx} \rangle \frac{\partial \{u_a\}}{\partial y_a} \, \mathrm{d}y_a}_{C_{f1}} + \underbrace{\frac{2}{\rho_b u_b^3} \int_0^h \langle \rho_a \rangle \{-u_a'' v_a''\} \frac{\partial \{u_a\}}{\partial y_a} \, \mathrm{d}y_a}_{C_{f2}}. \tag{2.10}$$

The skin-friction coefficient has been decomposed into two components, C_{f1} represents the direct molecular viscous dissipation, transforming the power of the skin-friction drag into heat, and C_{f2} represents the power converted into turbulent kinetic energy production induced by turbulent fluctuations, before being dissipated.

For practical reasons, (2.10) is reformulated back into the initial reference frame, and the direct viscous dissipation explicitly associated with the thermodynamic fluctuations is isolated. Thus the skin-friction drag is expressed as

$$C_f = \underbrace{\frac{2}{\rho_b u_b^3} \int_0^h \left\langle \mu \left(\frac{\partial u}{\partial y} + \frac{\partial v}{\partial x} \right) \right\rangle \frac{\partial \{u\}}{\partial y} \, \mathrm{d}y}_{C_{f1}} + \underbrace{\frac{2}{\rho_b u_b^3} \int_0^h \langle \rho \rangle \{-u'' v''\} \frac{\partial \{u\}}{\partial y} \, \mathrm{d}y}_{C_{f2}}, \tag{2.11}$$

where

$$C_{f1} = \underbrace{\frac{2}{\rho_b u_b^3} \int_0^h \langle \mu \rangle \frac{\partial \langle u \rangle}{\partial y} \frac{\partial \{u\}}{\partial y} \, \mathrm{d}y}_{C_{f1,m}} + \underbrace{\frac{2}{\rho_b u_b^3} \int_0^h \left\langle \mu' \frac{\partial u'}{\partial y} + \mu' \frac{\partial v'}{\partial x} \right\rangle \frac{\partial \{u\}}{\partial y} \, \mathrm{d}y}_{C_{f1,f}}. \tag{2.12}$$

Recalling the incompressible RD identity (1.2) (Renard & Deck 2016), similarities and differences are observed with the compressible formulation (2.11). In particular, as in the incompressible case, the skin-friction drag is decomposed into two branches, associated with molecular viscosity dissipation and TKE production. On the other hand differences can be found in the additional term $C_{f1,f}$ in (2.12) which embeds the viscosity variations. In compressible isothermal channel flows, direct viscous dissipation consists of $C_{f1,m}$ and $C_{f1,f}$, which are respectively dependent on the mean flow and thermodynamic fluctuations. In § 4.3, we apply classical compressibility transformation to take into account the mean density and viscosity variations and compare the contributions in the compressible cases to those in the incompressible ones.

2.2. *Correlation between wall heat flux and skin-friction drag coefficient*

Heat transfer in the compressible isothermal channel flow is taken into consideration in this subsection. The Reynolds-averaged energy equation incorporating the channel-flow hypotheses gives

$$\frac{\partial\langle\rho v(e+V^2/2)\rangle}{\partial y} = \frac{\partial}{\partial y}\left(K\frac{\partial\langle T\rangle}{\partial y}\right) - \frac{\partial\langle vp\rangle}{\partial y} + \frac{\partial\langle u\tau_{yx}\rangle}{\partial y} + \frac{\partial\langle v\tau_{yy}\rangle}{\partial y} + \frac{\partial\langle w\tau_{yz}\rangle}{\partial y} + \langle\rho fu\rangle, \tag{2.13}$$

where e and $V^2/2$ are respectively the internal energy and kinetic energy per unit mass, K is thermal conductivity, T is temperature, p is static pressure, w is spanwise velocity and τ_{yx}, τ_{yy}, τ_{yz} are viscous stresses respectively along the x-, y-, z-direction. Wall heat flux q_w is defined as the local power per unit area transferred between the wall and fluid, and calculated by $-K(\partial\langle T\rangle/\partial y)|_{wall}$. To obtain the wall heat flux q_w, we integrate (2.13) from the wall surface to the central plane, leading to

$$q_w = -\rho_b u_b h f. \tag{2.14}$$

Equation (2.14) shows that the heat transfer to the wall comes from the power done by the external body force, which is balanced by the skin-friction drag. Substituting (2.4) into (2.14) gives

$$q_w = -u_b\tau_w. \tag{2.15}$$

As for the wall heat flux coefficient B_q, it is defined to be $q_w/(\rho_w C_p u_\tau T_w)$, where subscript w denotes variables at the wall surface, C_p is the specific heat at constant pressure and u_τ is friction velocity defined as $\sqrt{(\tau_w/\rho_w)}$ (τ_w denotes the wall shear stress). Then we have

$$B_q = -\frac{0.5{M_b}^2(\gamma-1)}{(\rho_w u_\tau)/(\rho_b u_b)}C_f, \tag{2.16}$$

where M_b is the bulk Mach number based on the bulk velocity and the sound speed at wall temperature, and γ is the specific heat ratio. Equation (2.16) constitutes a direct relationship between B_q and C_f, allowing us to predict the wall heat flux coefficient and decompose it into different contributions, such as the skin-friction drag coefficient. Thus considering (2.11), B_q is also related to the statistical quantities across the whole wall layer, and no longer strongly dependent on the temperature gradient at the wall surface, which is difficult to accurately obtain.

3. Direct numerical simulation of compressible turbulent channel flows

Direct numerical simulations (DNSs) of compressible turbulent channel flows have been performed with a finite difference code, by solving the three-dimensional unsteady compressible Navier–Stokes equations. The convective terms are discretized with a modified seventh-order weighted compact nonlinear scheme (WCNS) (Nonomura & Fujii 2009; Nonomura, Iizuka & Fujii 2010; Nonomura *et al.* 2011). The viscous terms are evaluated with an eighth-order central difference scheme. A third-order total-variation-diminishing Runge–Kutta scheme (Jiang & Shu 1996) is adopted for the time integration, and the time step is set to ensure the Courant–Friedrichs–Lewy number is less than unity. A constant molecular Prandtl number Pr of 0.72 and specific heat ratio γ of 1.4 are used. To drive the channel flow, a body force is imposed in the streamwise direction, maintaining a constant mass flow rate (Huang *et al.* 1995).

We carry out five DNSs to investigate the effects of Reynolds and Mach number variation in supersonic isothermal channel flows. Details of the flow conditions, computational domains and grid resolutions are listed in table 1. In particular we carry out three simulations at a bulk Mach number $M_b = u_b/c_w = 1.5$ (where c_w is the speed of sound at wall temperature), and bulk Reynolds numbers $Re_b =$ 3000, 9400 and 20 000, respectively. As discussed in Modesti & Pirozzoli (2016), compressible wall-bounded flows can be compared to incompressible flow data at the matching equivalent Reynolds number. To this end we introduce the following mapping for the wall-normal coordinate (Huang *et al.* 1995; Trettel & Larsson 2016),

$$y_T(y) = \frac{(\langle\rho\rangle/\rho_w)^{1/2}}{\langle\mu\rangle/\mu_w} y, \tag{3.1}$$

and the transformed friction Reynolds number is defined accordingly (Modesti & Pirozzoli 2019),

$$Re_\tau^* = y_T(h)/\delta_v. \tag{3.2}$$

The modified wall distance in viscous units is indicated with a plus superscript, $y_T^+ = y_T/\delta_v$.

Based on the local and wall properties, we also define the semi-local friction velocity and viscous length scale as $u_\tau^* = \sqrt{(\rho_w/\langle\rho\rangle)}u_\tau$ and $\delta_v^* = (\langle\mu\rangle/\mu_w/\sqrt{\langle\rho\rangle/\rho_w})\delta_v$, respectively (Huang *et al.* 1995). In the first three cases, the transformed Reynolds numbers are $Re_\tau^* =$ 140, 400 and 800, respectively. Moreover we carry out two flow cases at $M_b = 3.0$, and $Re_b = 4880$ and 14 000 ($Re_\tau^* = 150$ and 400), respectively.

The computational domain for the cases at $M_b = 1.5$, $Re_b = 3000$ and $M_b = 3.0$, $Re_b = 4880$ is $L_x \times L_y \times L_z = 4\pi h \times 2h \times 3\pi h/2$. For the other cases simulated, the computational domain is set as $L_x \times L_y \times L_z = 2\pi h \times 2h \times \pi h$. According to del Álamo *et al.* (2004) and Lozano-Durán & Jiménez (2014), this computational domain is sufficiently large to reproduce accurate turbulent statistics in the current range of Re_τ. To prove the adequacy of the domain size, we check the two-point correlations both in the streamwise and spanwise directions, as discussed in appendix B. The computational domain is discretized using $N_x \times N_y \times N_z$ grid points in the x-, y- and z-directions, respectively. A uniform mesh spacing is employed in the spanwise and streamwise directions, whereas in the wall-normal direction the mesh is hyperbolically clustered towards the walls. The minimum and maximum wall-normal grid spacing in classical viscous units are $\Delta y^+_{min} \approx 0.5$ and $\Delta y^+_{max} \approx 10$ for all flow cases; Δx^+ and Δz^+

https://doi.org/10.1017/jfm.2019.499 Published online by Cambridge University Press

M_b	Re_b	Re_τ	Re^*_τ	$L_x \times L_y \times L_z$	$N_x \times N_y \times N_z$	Δy^+_{min}	Δy^+_{max}	Δx^+	Δz^+	$\Delta y^+_{T,min}$	$\Delta y^+_{T,max}$	Δx^+_T	Δz^+_T
1.5	3 000	220	140	$4\pi h \times 2h \times 3\pi h/2$	$280 \times 150 \times 200$	0.33	6.74	9.87	5.18	0.21	4.29	6.28	3.30
1.5	9 400	600	400	$2\pi h \times 2h \times \pi h$	$250 \times 200 \times 250$	0.60	14.00	15.08	7.54	0.40	9.33	10.05	5.03
1.5	20 000	1170	800	$2\pi h \times 2h \times \pi h$	$530 \times 450 \times 530$	0.59	11.66	13.87	6.94	0.40	7.97	9.48	4.74
3.0	4 880	450	150	$4\pi h \times 2h \times 3\pi h/2$	$500 \times 250 \times 420$	0.28	9.21	11.31	5.05	0.09	3.07	3.77	1.68
3.0	14 000	1160	400	$2\pi h \times 2h \times \pi h$	$500 \times 450 \times 500$	0.58	11.79	14.58	7.29	0.20	4.07	5.03	2.51

TABLE 1. Details of flow conditions, computational domains and grid resolutions.

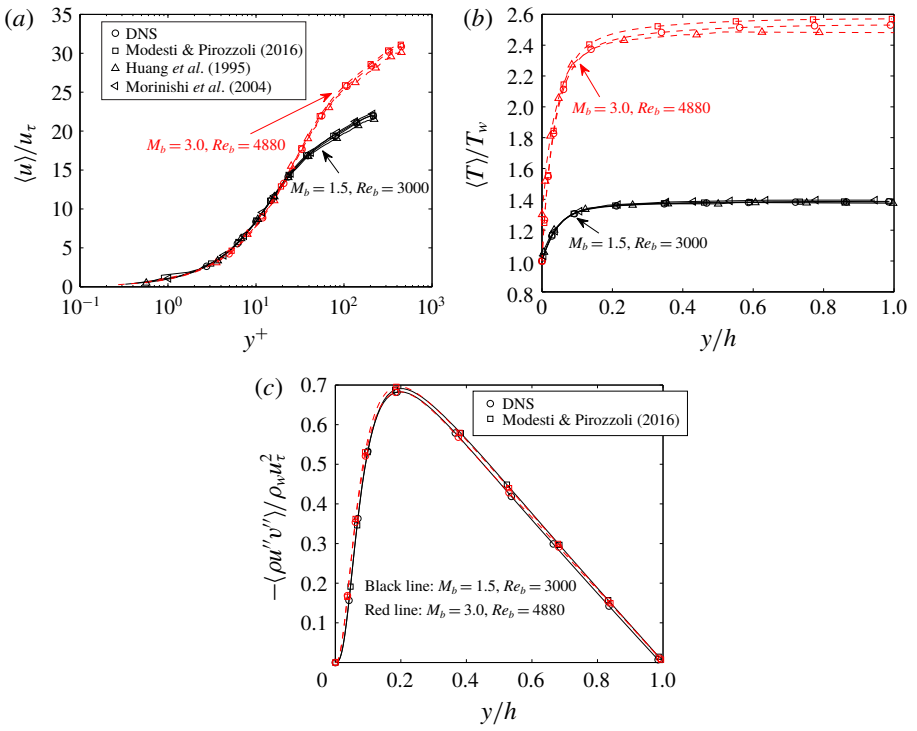

FIGURE 1. (Colour online) Profiles of (*a*) mean streamwise velocity, (*b*) temperature, (*c*) Reynolds shear stress for the two cases at $M_b = 1.5$, $Re_b = 3000$ and $M_b = 3.0$, $Re_b = 4880$.

are the uniform grid spacings in the streamwise and spanwise directions, respectively. Table 1 also gives the grid spacing normalized by the transformed Reynolds number (as in (3.2)), i.e. $\Delta y^+_{T,min} \lessapprox 0.5$, $\Delta y^+_{T,max} \lessapprox 10$, $\Delta x^+_T \lessapprox 10$ and $\Delta z^+_T \lessapprox 5$. Periodic boundary conditions are employed in the spanwise and streamwise directions, and isothermal no-slip conditions are imposed at the walls. The flow is initialized with a parabolic velocity profile with random perturbations superposed, and with uniform values of density and temperature (Modesti & Pirozzoli 2016).

DNS data at $M_b = 1.5$, $Re_b = 3000$ and $M_b = 3.0$, $Re_b = 4880$ are compared to flow statistics of Huang *et al.* (1995), Morinishi, Tamano & Nakabayashi (2004) and Modesti & Pirozzoli (2016). Figure 1 shows the profiles of mean streamwise velocity, temperature and Reynolds shear stress, which agree well with the previous studies. Flow cases at $M_b = 1.5$, $Re_b = 9400$ and $M_b = 1.5$, $Re_b = 20\,000$ are compared to approximately matching reference data of Modesti & Pirozzoli (2016) at $M_b = 1.5$, $Re_b = 7667$ and $M_b = 1.5$, $Re_b = 17\,000$, respectively, as shown in figure 2. Minor differences between the distributions are observed due to the difference in bulk Reynolds numbers, thus confirming the accuracy of the present dataset.

4. Results and discussion

The relations between the mean skin-friction drag coefficients and Reynolds numbers are plotted in figure 3, in which the mean skin-friction drag coefficients are directly calculated from the normal gradients of mean streamwise velocity at the wall. They are compared to the empirical correlation of incompressible turbulent

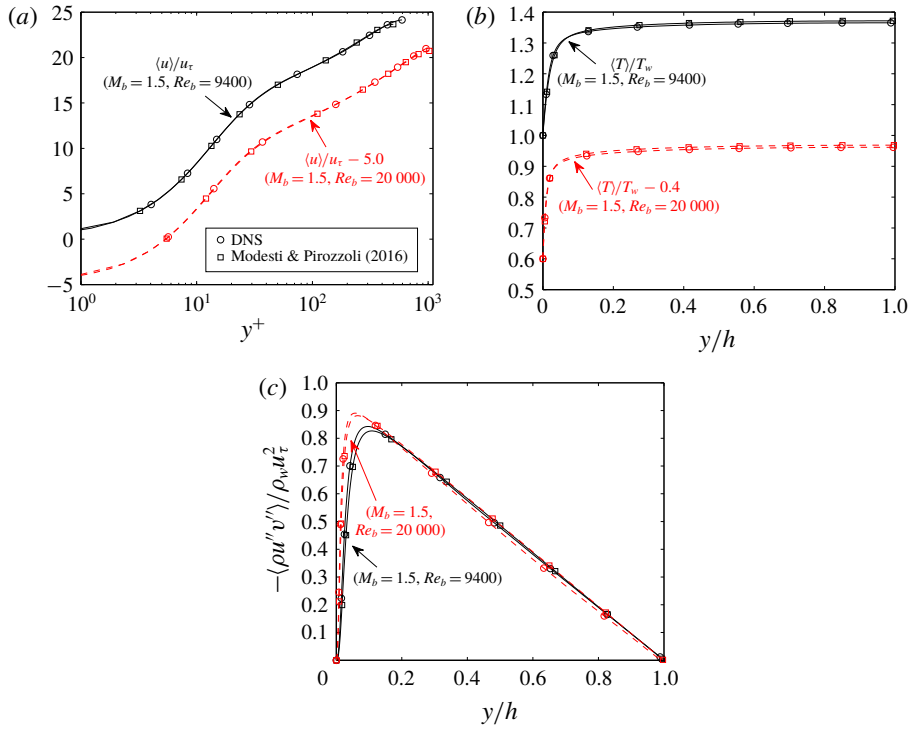

FIGURE 2. (Colour online) Profiles of (*a*) mean streamwise velocity, (*b*) temperature, (*c*) Reynolds shear stress for the two cases at $M_b = 1.5$, $Re_b = 9400$ and $M_b = 1.5$, $Re_b = 20\,000$.

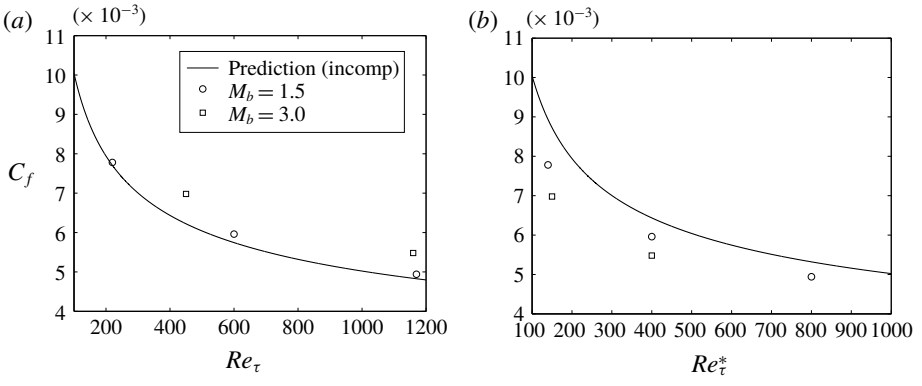

FIGURE 3. Mean skin-friction drag coefficients for compressible turbulent channel flows with regard to (*a*) Re_τ and (*b*) Re_τ^* compared with the incompressible empirical results.

channel flows given by Abe & Antonia (2016), $C_f = 2/(2.54\ln(Re_\tau) + 2.41)^2$. Both the friction Reynolds number Re_τ and the transformed Reynolds number Re_τ^* are used to check the $C_f - Re$ correlation. Figure 3(*a*,*b*) shows that the compressible friction coefficient increases for increasing Mach number, at given Re_τ, and using the equivalent Reynolds number Re_τ^* is not sufficient to account for the thermodynamic property variation effects.

M_b	Re_τ	Re_τ^*	$C_{f1,m}/C_f$	$C_{f1,f}/C_f$	C_{f1}/C_f	C_{f2}/C_f	Relative error
1.5	220	140	62.40 %	0.36 %	62.76 %	37.03 %	−0.21 %
1.5	600	400	51.59 %	0.30 %	51.89 %	47.03 %	−1.08 %
1.5	1170	800	45.63 %	0.26 %	45.89 %	51.29 %	−2.82 %
3.0	450	150	61.66 %	0.87 %	62.53 %	36.44 %	1.02 %
3.0	1160	400	49.81 %	0.73 %	50.54 %	46.84 %	−2.62 %

TABLE 2. Contributions of the decomposed skin-friction drag components.

According to the theory developed in § 2.1, the mean skin-friction drag coefficients are decomposed into three contributing constituents, $C_{f1,m}$, $C_{f1,f}$ and C_{f2}. Their proportions in terms of the total skin-friction drag coefficient, as well as C_{f1}/C_f ($C_{f1} = C_{f1,m} + C_{f1,f}$), are listed in table 2. The relative errors, $[(C_{f1} + C_{f2}) - C_f]/C_f$, are confined within $\pm 2.82\,\%$, indicating that the decomposition method is fairly reliable in estimating the mean skin-friction drag coefficients. The decomposed results suggest that at low Reynolds numbers the direct viscous dissipation C_{f1} is the predominant drag component, reaching approximately 63 % at $Re_\tau^* \approx 150$. As the Reynolds number increases, the predominance of C_{f1} is gradually overtaken by the component of TKE production C_{f2}. This phenomenon is consistent with the study of Renard & Deck (2016) in incompressible flows. At the same Re_τ^*, varying the bulk Mach number M_b from 1.5 to 3.0 does not have any significant influence on the decomposed results.

To further quantify the effects of Reynolds and Mach number on the mean skin-friction drag generation, in the following two subsections we will investigate the profiles of C_{f1}/C_f and C_{f2}/C_f across the channel.

4.1. *Effects of Reynolds number on the mean skin-friction drag generation*

The formulas for C_{f1}/C_f and C_{f2}/C_f are rewritten in the intrinsic scales, *viz.*

$$\frac{C_{f1}}{C_f} = \int_0^{Re_\tau} \frac{u_\tau}{u_b} \left\langle \frac{\mu}{\mu_w} \left(\frac{\partial u^+}{\partial y^+} + \frac{\partial v^+}{\partial x^+} \right) \right\rangle \frac{\partial \{u\}^+}{\partial y^+} \, \mathrm{d}y^+, \tag{4.1}$$

$$\frac{C_{f2}}{C_f} = \int_0^{Re_\tau} \frac{u_\tau}{u_b} \frac{\langle \rho \rangle}{\rho_w} \{-u''v''\}^+ \frac{\partial \{u\}^+}{\partial y^+} \, \mathrm{d}y^+, \tag{4.2}$$

where the superscript $+$ denotes normalization with viscous variables.

To assess the effects of Reynolds number on the mean skin-friction drag generation, profiles of the pre-multiplied integrands in (4.1) and (4.2) are plotted in figures 4 and 5, respectively, as a function of viscous wall distance y^+ ($= y/\delta_v$, $\delta_v = \nu_w/u_\tau$). Integrating the pre-multiplied integrands over the wall layer gives the corresponding proportions of C_{f1} and C_{f2} in the total skin-friction drag.

As shown in figure 4, the pre-multiplied integrands of C_{f1}/C_f share similarity in curve shape and peak at almost the same y^+ location for the flows at the same bulk Mach number. Their peaks are reduced when we increase the Reynolds number, indicating a negative correlation between the contribution of viscous dissipation and the Reynolds number. The contribution of viscous dissipation is mainly located in the near-wall region, for instance $y^+ \lessapprox 30$, as seen in figure 4.

As for the pre-multiplied integrands of C_{f2}/C_f, a similar feature of the peak location and peak value is observed for flows at the same bulk Mach number, as

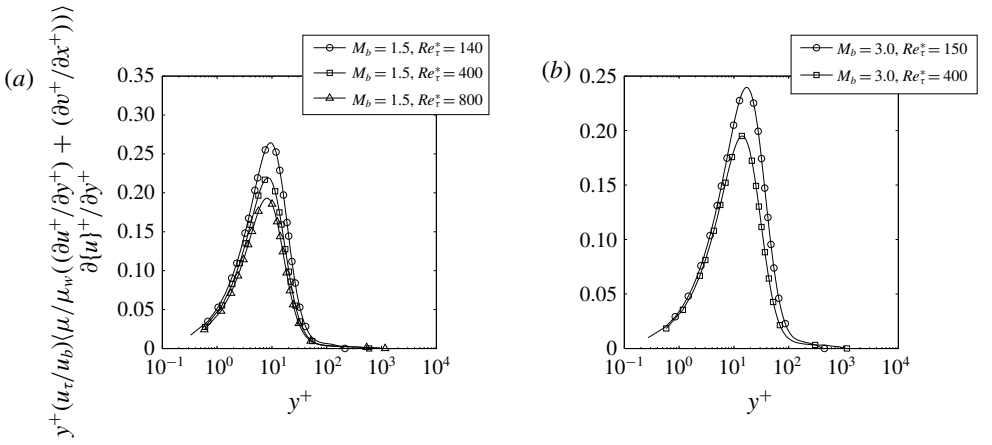

FIGURE 4. Pre-multiplied integrands of C_{f1}/C_f as a function of y^+. (*a*) $M_b = 1.5$ and (*b*) $M_b = 3.0$.

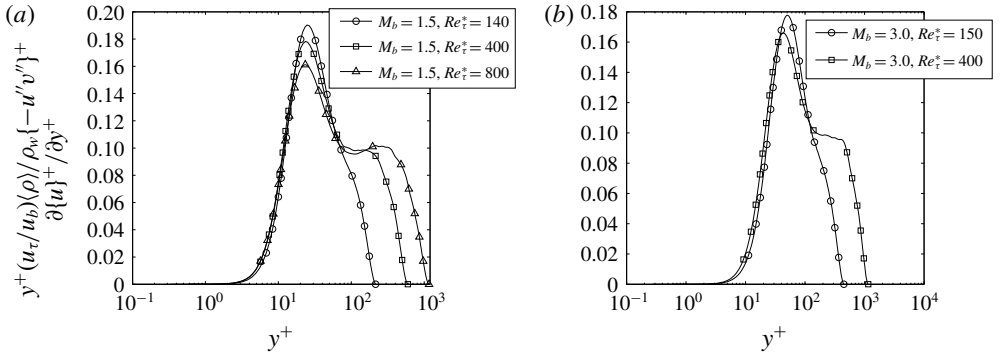

FIGURE 5. Pre-multiplied integrands of C_{f2}/C_f as a function of y^+. (*a*) $M_b = 1.5$ and (*b*) $M_b = 3.0$.

displayed in figure 5. The majority of TKE-production contributions are generated in the region where $y^+ \gtrapprox 10$. The profiles in the near-wall region ($y^+ \lessapprox 30$) collapse well onto a single curve, indicating that the Reynold number has little impact on the TKE production in this region. A secondary peak emerges in the outer layer as the Reynolds number increases, which is ascribed to the generation of the large-scale turbulent motions. The existence of large-scale turbulent motions in the outer layers at large Reynolds numbers has been confirmed in many studies, e.g. Kim & Adrian (1999), Balakumar & Adrian (2007), Hutchins & Marusic (2007*a*), Monty *et al.* (2009) and Lee & Sung (2011). The large-scale turbulent motions lead to the generation of large amounts of turbulent kinetic energy in the outer layer, and correspondingly contribute to the generation of the skin-friction drag. Meanwhile, large-scale turbulent motions have actions that modulate the small-scale turbulent motions in the near-wall region (Hutchins & Marusic 2007*b*), which leads to the redistribution of turbulent kinetic energy between the near-wall region and the outer region. This possibly explains the decrease of the (first) peak values in figure 5 as the Reynolds number increases.

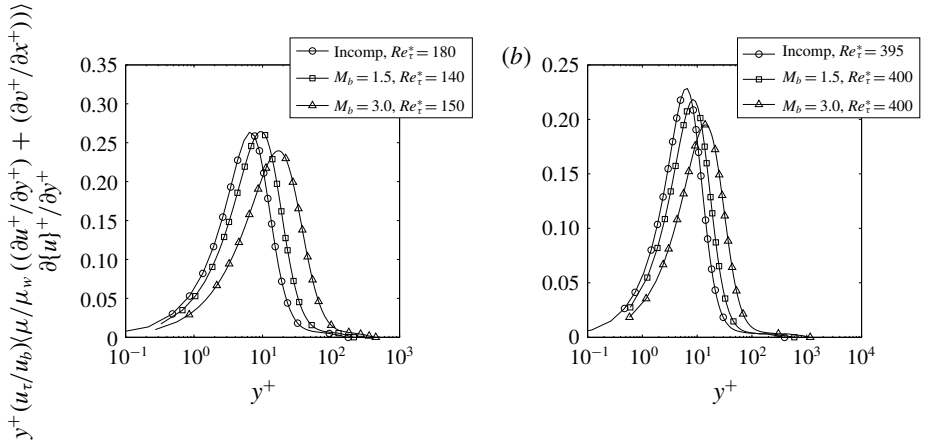

FIGURE 6. Pre-multiplied integrands of C_{f1}/C_f as a function of y^+. (*a*) $Re_\tau^* \approx 150$ and (*b*) $Re_\tau^* \approx 400$.

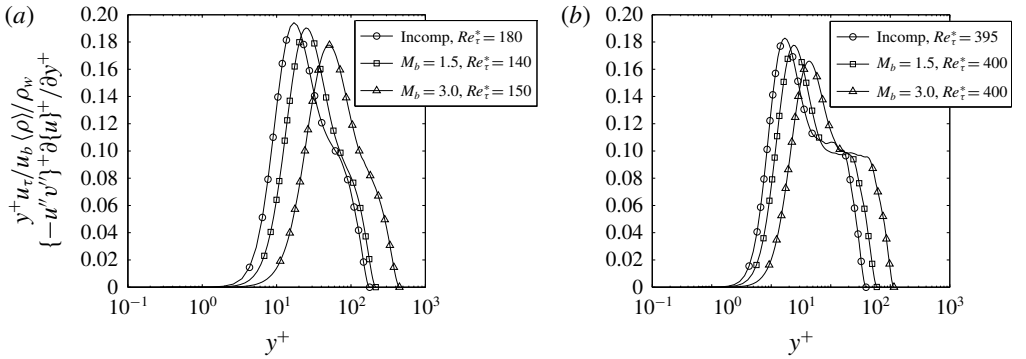

FIGURE 7. Pre-multiplied integrands of C_{f2}/C_f as a function of y^+. (*a*) $Re_\tau^* \approx 150$ and (*b*) $Re_\tau^* \approx 400$.

4.2. *Effects of Mach number on the mean skin-friction drag generation*

Keeping the transformed Reynolds number the same, we plot profiles of the pre-multiplied integrands of C_{f1}/C_f and C_{f2}/C_f in figures 6 and 7, respectively, aiming to discuss the effects of Mach number on the mean skin-friction drag generation. Two incompressible turbulent channel flows at $Re_\tau = 180$ and 395 (Moser, Kim & Mansour 1999) are also included for discussion.

The area below the integrands describes the contributions of molecular viscous dissipation or TKE production to the total skin-friction drag. If the transformed Reynolds number is the same, varying the bulk Mach number from 1.5 to 3.0 has little influence on the total area below the integrands, which corresponds to the results in table 2. However, as the Mach number increases, the peaks of the pre-multiplied integrands apparently shift away from the wall as shown in figures 6 and 7. It indicates that the thermodynamic property variations have non-negligible impacts on the distributions of both decomposed constituents respectively related to the molecular viscous dissipation and the TKE production. Figure 8 quantifies the variation of dynamic viscosity with respect to the Mach number. It is a vital parameter in the viscous dissipation distributions and is positively relevant to the temperature through Sutherland's law. In turbulent isothermal channel flows, the

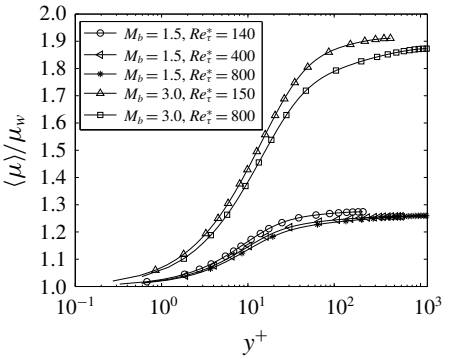

FIGURE 8. Profiles of dynamic viscosity.

viscosity coefficient increases dramatically in a wider region of y^+, as we increase the Mach number. For instance, the dramatic rise of $\langle\mu\rangle/\mu_w$ is limited in the region of $y^+ \lessapprox 30$ at $M_b = 1.5$; if we change the bulk Mach number to 3.0, this region is extended to $y^+ \lessapprox 100$. Thus the maximum of the direct viscous dissipation contribution shows up at a larger y^+. Correspondingly, the dissipation is no longer limited in the inner region ($y^+ \lessapprox 30$), as the bulk Mach number reaches high values, which means that Mach number increase leads to the reinforcement of dissipative effect across the channel and thus the intensification of heat transfer.

4.3. *'Compressible' contributions to the skin-friction drag generation*

As mentioned in § 2.1, C_f is split into $C_{f1,m}$, $C_{f1,f}$ and C_{f2}, where $C_{f1,f}$ is generated due to the fluid compressibility as it contains viscosity fluctuations, and it cannot be transformed into an 'incompressible' contribution. Whereas, the effect of density and viscosity variations on $C_{f1,m}$ and C_{f2} can be accounted for by applying the compressibility transformations to the streamwise velocity and Reynolds shear stress, *viz.*

$$u_T^+ = \int_0^{u^+} \frac{\langle\mu\rangle}{\mu_w}\frac{\mathrm{d}y_T^+}{\mathrm{d}y^+}\,\mathrm{d}u^+ \quad \text{and} \quad \tau_T^+ = \frac{-\langle\rho u'' v''\rangle}{\rho_w u_\tau^2}. \tag{4.3a,b}$$

These transformations should allow us to obtain the Mach-number-invariant contributions of $C_{f1,m}$ and C_{f2} to the total skin-friction drag coefficient.

Substituting these transformations in (2.12) and (2.11),

$$\frac{C_{f1,m}}{C_f} = \int_{y=0}^{y=h} \frac{\partial\langle u\rangle_T^+}{\partial y_T^+}\frac{\partial\{u\}_T^+}{\partial y_T^+}\frac{u_\tau^*}{u_b}\,\mathrm{d}y_T^+ + \int_{y=0}^{y=h} \frac{\partial\langle u\rangle_T^+}{\partial y_T^+}\frac{\partial\{u\}_T^+}{\partial y_T^+}\frac{u_\tau^*}{u_b}\frac{y_T^+}{\delta_\nu^*}\,\mathrm{d}\delta_\nu^*, \tag{4.4}$$

$$\frac{C_{f2}}{C_f} = \int_{y=0}^{y=h} \tau_T^+\frac{\partial\{u\}_T^+}{\partial y_T^+}\frac{u_\tau^*}{u_b}\,\mathrm{d}y_T^+ + \int_{y=0}^{y=h} \tau_T^+\frac{\partial\{u\}_T^+}{\partial y_T^+}\frac{u_\tau^*}{u_b}\frac{y_T^+}{\delta_\nu^*}\,\mathrm{d}\delta_\nu^*. \tag{4.5}$$

The integrands in (4.4) and (4.5) depend both on the Mach and Reynolds numbers through the ratio u_τ^*/u_b. In order to isolate the effect of mean density and viscosity variations and obtain universal distributions across Mach and Reynolds numbers, we follow the $C_f^{1.5}$ scaling as in Fan, Cheng & Li (2019) for incompressible channel flows. To this end, we divide the first terms on the right-hand sides of (4.4) and (4.5) by

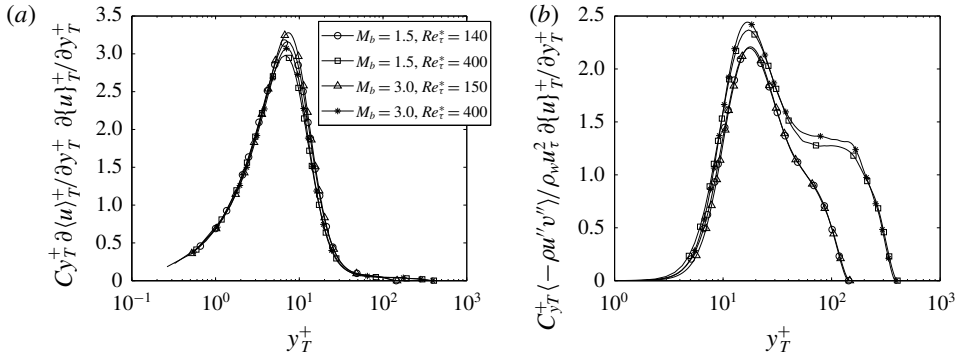

FIGURE 9. Pre-multiplied integrands of (*a*) $(C_{f1,m}/C_f^{1.5})_{incomp}$ and (*b*) $(C_{f2}/C_f^{1.5})_{incomp}$ as a function of y_T^+.

$\sqrt{\rho_w/\rho_b(u_\tau/u_b)^2}$ (recall $C_f = 2\rho_w/\rho_b(u_\tau/u_b)^2$), and recast (4.4) and (4.5) as

$$\frac{C_{f1,m}}{C_f^{1.5}} = C\int_0^{Re^*_\tau} \frac{\partial\langle u\rangle^+_T}{\partial y^+_T}\frac{\partial\{u\}^+_T}{\partial y^+_T}\,\mathrm{d}y^+_T + C\int_0^{Re^*_\tau} \frac{\partial\langle u\rangle^+_T}{\partial y^+_T}\frac{\partial\{u\}^+_T}{\partial y^+_T}\left(\sqrt{\frac{\rho_b}{\langle\rho\rangle}} - 1 + \frac{y^+_T}{\delta^*_v}\sqrt{\frac{\rho_b}{\langle\rho\rangle}}\frac{\mathrm{d}\delta^*_v}{\mathrm{d}y^+_T}\right)\mathrm{d}y^+_T, \tag{4.6}$$

$$\frac{C_{f2}}{C_f^{1.5}} = C\int_0^{Re^*_\tau} \tau^+_T\frac{\partial\{u\}^+_T}{\partial y^+_T}\,\mathrm{d}y^+_T + C\int_0^{Re^*_\tau} \tau^+_T\frac{\partial\{u\}^+_T}{\partial y^+_T}\left(\sqrt{\frac{\rho_b}{\langle\rho\rangle}} - 1 + \frac{y^+_T}{\delta^*_v}\sqrt{\frac{\rho_b}{\langle\rho\rangle}}\frac{\mathrm{d}\delta^*_v}{\mathrm{d}y^+_T}\right)\mathrm{d}y^+_T, \tag{4.7}$$

where $C = 1/(\sqrt{2})$.

Given the generally good accuracy of the compressibility transformation used (Modesti & Pirozzoli 2016), the first terms in (4.6) and (4.7) are expected to be Mach-number invariant and they are referred to as the incompressible components, and labelled as $(C_{f1,m}/C_f^{1.5})_{incomp}$ and $(C_{f2}/C_f^{1.5})_{incomp}$. Distributions of these pre-multiplied integrands are given in figure 9, in which good collapse is observed for cases at the same transformed Reynolds number Re^*_τ. Areas beneath the distributions denote the specific values of $(C_{f1,m}/C_f^{1.5})_{incomp}$ and $(C_{f2}/C_f^{1.5})_{incomp}$, respectively. The maximum mismatch of both $(C_{f1,m}/C_f^{1.5})_{incomp}$ and $(C_{f2}/C_f^{1.5})_{incomp}$ for cases at the same Re^*_τ but different M_b is within $\pm 1.8\,\%$, which indicates that the influence of the thermodynamic property variations on each contribution has been removed, as expected. In addition, coincidences of the peak locations at $y_T^+ \approx 6.5$ and 17.0 are observed in figures 9(*a*) and 9(*b*), respectively, regardless of the variation of Reynolds number and Mach number. This phenomenon is interestingly consistent with the results for incompressible boundary layers (figure 5 in Renard & Deck's (2016) paper) and incompressible channel flows (figures 4*b* and 5*b* in Fan *et al.*'s (2019) paper).

Furthermore, we note that additional terms appear which depend on the mean density and viscosity, suggesting that compressibility transformations can only approximately account for mean thermodynamic property variation effects on each contributing term. The second terms in equations (4.6) and (4.7) are therefore denoted as $(C_{f1,m}/C_f^{1.5})_{comp}$ and $(C_{f2}/C_f^{1.5})_{comp}$, as they cannot be exactly written

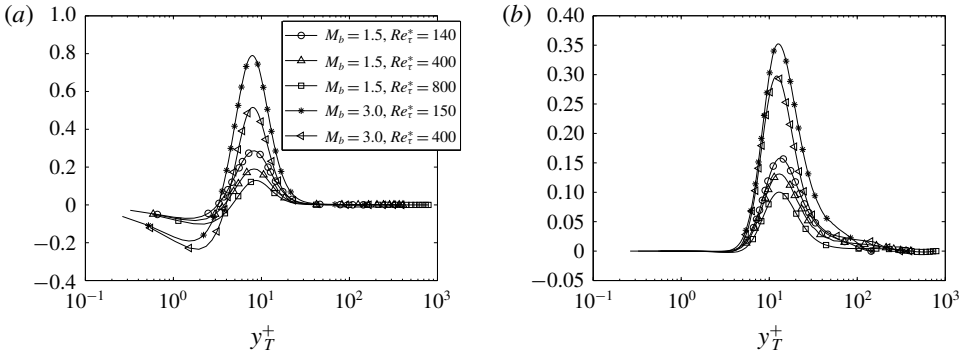

FIGURE 10. Pre-multiplied integrands of (*a*) $(C_{f1,m}/C_f^{1.5})_{comp}$ and (*b*) $(C_{f2}/C_f^{1.5})_{comp}$ as a function of y_T^+.

in terms of transformed variables and they should be regarded as deviations from the standard compressibility transformation. Profiles of the pre-multiplied integrands of $(C_{f1,m}/C_f^{1.5})_{comp}$ and $(C_{f2}/C_f^{1.5})_{comp}$ are plotted in figure 10. Areas beneath the curves explicitly indicate the total values and the figure shows that the relative contributions of $(C_{f1,m}/C_f^{1.5})_{comp}$ and $(C_{f2}/C_f^{1.5})_{comp}$ are small compared to $(C_{f1,m}/C_f^{1.5})_{incomp}$ and $(C_{f2}/C_f^{1.5})_{incomp}$. We note that the peak values of $(C_{f1,m}/C_f^{1.5})_{comp}$ and $(C_{f2}/C_f^{1.5})_{comp}$ occur in the near-wall region ($y_T^+ < 30$ for instance) where density and viscosity variations are higher, and figure 10 also suggests that these contributions becomes negligible for increasing Re_τ^*. In order to quantify the total 'compressible' contribution to the skin-friction drag coefficient we introduce

$$\left(\frac{C_f}{C_f^{1.5}}\right)_{comp} = \left(\frac{C_{f1,m}}{C_f^{1.5}}\right)_{comp} + \left(\frac{C_{f2}}{C_f^{1.5}}\right)_{comp} + \frac{C_{f1,f}}{C_f^{1.5}}, \tag{4.8}$$

and we introduce the normalized deviation with respect to the total friction coefficient

$$R_{comp} = \frac{(C_f/C_f^{1.5})_{comp}}{(C_f/C_f^{1.5})_{incomp} + (C_f/C_f^{1.5})_{comp}}. \tag{4.9}$$

Table 3 shows the different contributions to the skin-friction drag coefficient and highlights that the terms $(C_{f1,m}/C_f^{1.5})_{comp}$, $(C_{f2}/C_f^{1.5})_{comp}$, and $C_{f1,f}/C_f^{1.5}$ are negligible compared the other components. In particular the term $(C_{f1,m}/C_f^{1.5})_{comp}$, associated with deviations from compressibility transformations for the velocity, is found to be close to zero for all flow cases, whereas the term $(C_{f2}/C_f^{1.5})_{comp}$, associated with deviations from compressibility transformations for the Reynolds stress is found to be larger but decreases with Re_τ^* increasing and it is barely 3 % at $M_b = 3$, $Re_\tau^* = 400$.

As for the exactly transformed components, they are compared to those of incompressible channel flows in figure 11. Statistical data of the incompressible channel flows at $Re_\tau^* = 180$, 550, 1000, 2000, 5200 are used (Lee & Moser 2015). For the incompressible cases, in contrast with the constancy of $C_{f1,RD}/C_f^{1.5} (\approx 6.5)$, $C_{f2,RD}/C_f^{1.5}$ has a logarithmic relationship with Re_τ^*, well fitted by $C_{f2,RD}/C_f^{1.5} \approx 1.87 \ln(Re_\tau^*) - 5.29$. This conclusion is consistent with the findings for incompressible flows of Laadhari (2007), Abe & Antonia (2016), Renard & Deck (2016) and Fan *et al.* (2019). As for the five cases simulated in the present study, the results of $(C_{f1,m}/C_f^{1.5})_{incomp}$ and $(C_{f2}/C_f^{1.5})_{incomp}$ agree fairly well with the incompressible

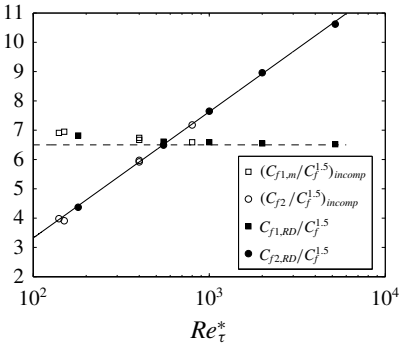

FIGURE 11. Distributions of $(C_{f1,m}/C_f^{1.5})_{incomp}$ and $(C_{f2}/C_f^{1.5})_{incomp}$ with regard to Re_τ^* in contrast with the results of incompressible channel flows.

M_b	Re_τ^*	$\left(\frac{C_{f1,m}}{C_f^{1.5}}\right)_{incomp}$	$\left(\frac{C_{f1,m}}{C_f^{1.5}}\right)_{comp}$	$\left(\frac{C_{f2}}{C_f^{1.5}}\right)_{incomp}$	$\left(\frac{C_{f2}}{C_f^{1.5}}\right)_{comp}$	$\frac{C_{f1,f}}{C_f^{1.5}}$	R_{comp}
1.5	140	6.91	0.16	3.98	0.21	0.04	3.62 %
1.5	400	6.67	0.00	5.92	0.18	0.04	1.68 %
1.5	800	6.59	−0.10	7.18	0.12	0.04	0.40 %
3.0	150	6.95	0.42	3.91	0.45	0.10	8.13 %
3.0	400	6.74	−0.02	5.97	0.36	0.10	3.25 %

TABLE 3. 'Incompressible' and 'compressible' contributions to the total skin-friction drag coefficient.

empirical rules, which confirms that the Trettel & Larsson (2016) transformation of velocity and Reynolds stress can accurately take into account the effect of density and viscosity variations.

4.4. *Wall heat flux coefficient*

Wall heat flux coefficient is an important wall property, which can be directly calculated by

$$B_{q,local} = -\frac{1}{Re_b Pr \rho_w u_\tau/(\rho_b u_b)} \left.\frac{\partial T/T_w}{\partial y/h}\right|_{y=0}. \tag{4.10}$$

In § 2.2, we derive an exact relation between the wall heat flux coefficient and the skin-friction drag coefficient. The relation in (2.16) offers a means to predict B_q from C_f, termed $B_{q,integral}$. Results of $B_{q,integral}$, $B_{q,local}$ and their relative errors, $(B_{q,integral} - B_{q,local})/B_{q,local}$, are listed in table 4. Fairly good agreements are observed in table 4, validating the accuracy of the (2.16).

The exact relation between the wall heat flux coefficient and the skin-friction drag coefficient in (2.16) indicates a similarity between the heat transfer and the momentum transport near the wall. This allows us to decompose the wall heat flux from the perspective of energy budget. Therefore, similar to the decomposition of the skin-friction drag, the wall heat transfer may be related to the molecular viscous dissipation and the turbulent kinetic energy production. Correspondingly, Reynolds and Mach number effects on the wall heat flux can be evaluated, as well. One of the advantages of (2.16) is that it allows for the physical interpretation and prediction of

M_b	Re_τ^*	$B_{q,integral}$	$B_{q,local}$	Relative error
1.5	140	-4.80×10^{-2}	-4.70×10^{-2}	2.23 %
1.5	400	-4.19×10^{-2}	-4.11×10^{-2}	1.97 %
1.5	800	-3.80×10^{-2}	-3.70×10^{-2}	2.70 %
3.0	150	-1.35×10^{-1}	-1.37×10^{-1}	−1.53 %
3.0	400	-1.19×10^{-1}	-1.16×10^{-1}	2.24 %

TABLE 4. Wall heat flux coefficients at five operation conditions.

the wall heat flux coefficient based on turbulence quantities across the wall layer in turbulent channel flows.

5. Conclusions

We focus on the decomposition of mean skin-friction drag in compressible turbulent channel flows. Firstly, we generalize the original RD identity (Renard & Deck 2016) to a compressible form, obtaining two contributing components C_{f1} and C_{f2}, respectively associated with: (i) power of the friction transformed into heat via direct molecular viscous dissipation, and (ii) power converted into turbulent kinetic-energy production. Unlike the original RD identity, we further split C_{f1} into two parts, $C_{f1,m}$ and $C_{f1,f}$, representing the contributions of the mean flow and the thermodynamic fluctuations, respectively.

Secondly, we investigate the Reynolds number dependence of the skin-friction contributions due to molecular viscosity and the TKE production. At low Reynolds number C_{f1} is dominant, whereas C_{f2} becomes dominant for increasing equivalent Reynolds number Re_τ^*, representing more than 50 % of the total skin-friction coefficient.

Thirdly, we quantify the effect of density and viscosity variations on the skin-friction coefficient by using Trettel & Larsson's (2016) transformation to separate the 'incompressible' and 'compressible' contributions. The 'incompressible' contributions, $(C_{f1,m}/C_f^{1.5})_{incomp}$ and $(C_{f2}/C_f^{1.5})_{incomp}$, are found to be comparable to the equivalent terms in incompressible turbulent channel flows (Fan *et al.* 2019), i.e. $(C_{f1,m}/C_f^{1.5})_{incomp} \approx 6.5$ and $(C_{f2}/C_f^{1.5})_{incomp} \approx 1.87\ln(Re_\tau^*) - 5.29$. Upon application of the compressibility transformation, additional terms appear, which cannot be cast as equivalent incompressible contributions and constitute the total 'compressible' contribution together with $C_{f1,f}$, representing the thermodynamic fluctuations. The total 'compressible' contribution to C_f, mostly associated with an excess of TKE production, is quite significant at low Reynolds numbers (up to 8 % at $M_b = 3.0$, $Re_\tau^* = 150$), whereas it becomes negligible at sufficiently large Re_τ^* and low M_b (barely 0.4 % at $M_b = 1.5$, $Re_\tau^* = 800$), suggesting that Morkovin's hypothesis holds and the effect of thermodynamic property variations can be accounted for simply by using compressibility transformations.

In addition, we derive and validate an exact relationship between the wall heat flux coefficient and the skin-friction drag coefficient, which allows us to relate the heat flux coefficient to the turbulence quantities across the wall layer in turbulent channel flows.

Acknowledgements

The funding support of National Natural Science Foundation of China (under the grant no. 11772194) is acknowledged. We also thank Tianhe-2 and the Center for

High Performance Computing at Shanghai Jiao Tong University for supporting the large-scale computations.

Appendix A. Skin-friction decomposition in compressible flat-plate boundary layers

For the compressible turbulent boundary layers, Reynolds number is characterized by free-stream velocity u_∞, free-stream density ρ_∞, boundary-layer thickness δ and dynamic viscosity at free-stream temperature μ_∞. Three assumptions are made: (i) no-slip conditions at the wall surfaces; (ii) statistical homogeneity in the spanwise (z-) direction; (iii) no additional body force. Then the Reynolds-averaged momentum equation in the streamwise (x-) direction is formulated as

$$\frac{\partial\langle\rho u\rangle}{\partial t}+\frac{\partial\langle\rho uu\rangle}{\partial x}+\frac{\partial\langle\rho uv\rangle}{\partial y}=-\frac{\partial\langle p\rangle}{\partial x}+\left(\frac{\partial\langle\tau_{xx}\rangle}{\partial x}+\frac{\partial\langle\tau_{yx}\rangle}{\partial y}\right), \tag{A 1}$$

where τ_{xx} is the normal stress in the x-direction.

Following the derivations in § 2.1, the mean skin-friction drag coefficient can be expressed in the absolute reference frame

$$\begin{aligned} C_f = &\underbrace{\frac{2}{\rho_\infty u_\infty^3}\int_0^\delta \langle\tau_{yx}\rangle\frac{\partial\{u_a\}}{\partial y_a}\,\mathrm{d}y_a}_{C_{f1}}+\underbrace{\frac{2}{\rho_\infty u_\infty^3}\int_0^\delta \langle\rho_a\rangle\{-u_a''v_a''\}\frac{\partial\{u_a\}}{\partial y_a}\,\mathrm{d}y_a}_{C_{f2}}\\ &+\underbrace{\frac{2}{\rho_\infty u_\infty^3}\int_0^\delta \langle\rho_a\rangle\frac{D\{K_a\}}{Dt_a}\,\mathrm{d}y_a}_{C_{f3}}\\ &-\underbrace{\frac{2}{\rho_\infty u_\infty^3}\int_0^\delta \{u_a\}\frac{\partial}{\partial(x_a+u_\infty t_a)}(\langle\tau_{xx}\rangle-\langle\rho_a\rangle\{u_a''u_a''\}-\langle p_a\rangle)\,\mathrm{d}y_a}_{C_{f4}}. \end{aligned} \tag{A 2}$$

Four contributing constituents are obtained: C_{f1} and C_{f2} represent the direct viscous dissipation and turbulence 'dissipation' into turbulent kinetic-energy production, respectively; C_{f3} represents the variation of mean streamwise kinetic energy with time, e.g. the time rate of fluid kinetic energy transferred from the moving wall in the absolute frame; C_{f4} is created by the streamwise heterogeneity, which had better be substituted with local information, in the case that streamwise derivatives are not contained in the database or are unfeasible to obtain (Mehdi & White 2011).

Finally, equation (A 2) is allowed to be written equivalently in the wall-attached reference frame for the convenience of calculation

$$\begin{aligned} C_f = &\underbrace{\frac{2}{\rho_\infty u_\infty^3}\int_0^\delta \langle\tau_{yx}\rangle\frac{\partial\{u\}}{\partial y}\,\mathrm{d}y}_{C_{f1}}+\underbrace{\frac{2}{\rho_\infty u_\infty^3}\int_0^\delta \langle\rho\rangle\{-u''v''\}\frac{\partial\{u\}}{\partial y}\,\mathrm{d}y}_{C_{f2}}\\ &+\underbrace{\frac{2}{\rho_\infty u_\infty^3}\int_0^\delta \langle\rho\rangle(\{u\}-u_\infty)\frac{\mathrm{D}\{u\}}{\mathrm{D}t}\,\mathrm{d}y}_{C_{f3}}\\ &-\underbrace{\frac{2}{\rho_\infty u_\infty^3}\int_0^\delta (\{u\}-u_\infty)\frac{\partial}{\partial x}(\langle\tau_{xx}\rangle-\langle\rho\rangle\{u''u''\}-\langle p\rangle)\,\mathrm{d}y}_{C_{f4}}. \end{aligned} \tag{A 3}$$

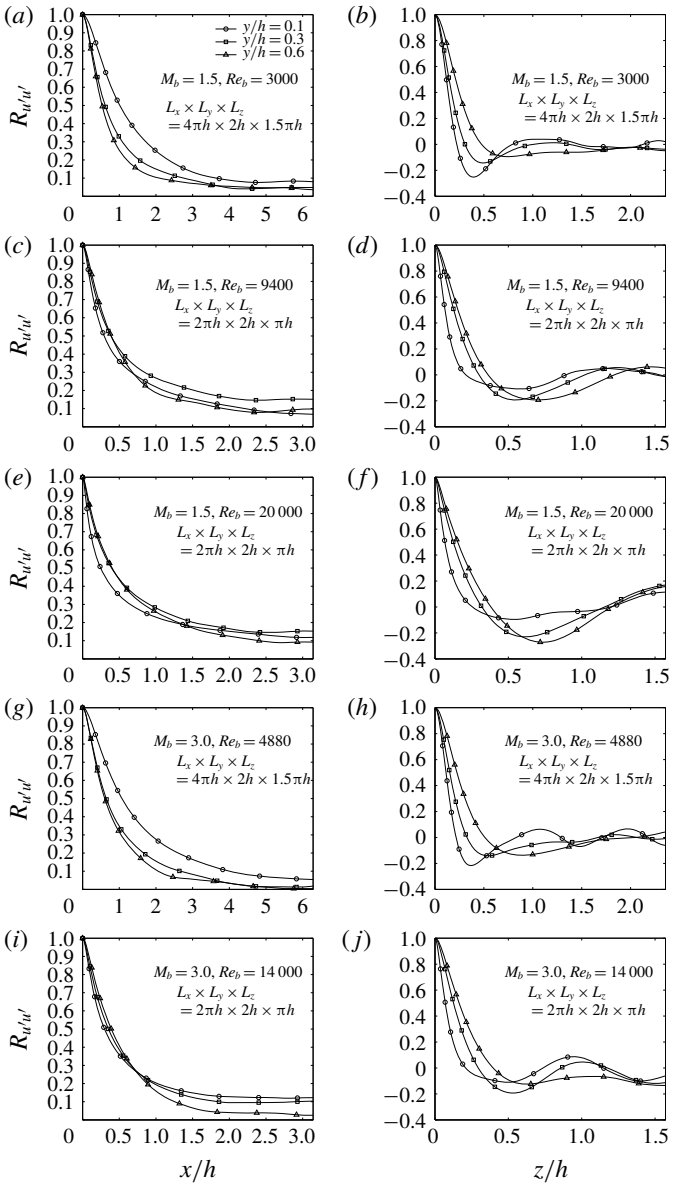

FIGURE 12. Streamwise and spanwise two-point correlations for streamwise velocity fluctuation $R_{u'u'}$ for five channel-flow cases.

Appendix B. Two-point correlations of the streamwise velocity fluctuation

To prove the adequacy of the domain size, we check the two-point correlations of the streamwise velocity fluctuation, $R_{u'u'}$, both in the streamwise and spanwise directions, with the designated computational domain in § 3, as displayed in figure 12.

Figure 12(*a*,*c*,*e*,*g*,*i*) shows $R_{u'u'}$ in the streamwise direction, and figure 12(*b*,*d*,*f*,*h*,*j*) shows $R_{u'u'}$ in the spanwise direction. It can be seen that the correlations are limited to small values at large separations, indicating that the domain sizes are sufficiently long (wide).

REFERENCES

ABE, H. & ANTONIA, R. A. 2016 Relationship between the energy dissipation function and the skin friction law in a turbulent channel flow. *J. Fluid Mech.* **798**, 140–164.

DEL ÁLAMO, J. C., JIMÉNEZ, J., ZANDONADE, P. & MOSER, R. D. 2004 Scaling of the energy spectra of turbulent channels. *J. Fluid Mech.* **500**, 135–144.

BALAKUMAR, B. J. & ADRIAN, R. J. 2007 Large- and very-large-scale motions in channel and boundary-layer flows. *Phil. Trans. R. Soc. Lond.* A **365** (1852), 665–681.

BANNIER, A., GARNIER, É. & SAGAUT, P. 2015 Riblet flow model based on an extended FIK identity. *Flow Turbul. Combust.* **95** (2-3), 351–376.

DECK, S., RENARD, N., LARAUFIE, R. & WEISS, P. É 2014 Large-scale contribution to mean wall shear stress in high-Reynolds-number flat-plate boundary layers up to $Re_\theta = 13\,650$. *J. Fluid Mech.* **743**, 202–248.

VAN DRIEST, E. R. 1951 Turbulent boundary layer in compressible fluids. *J. Aero. Sci.* **18** (3), 145–160.

DUAN, L., BEEKMAN, I. & MARTIN, M. P. 2010 Direct numerical simulation of hypersonic turbulent boundary layers. Part 2. Effect of wall temperature. *J. Fluid Mech.* **655**, 419–445.

DUAN, L., BEEKMAN, I. & MARTIN, M. P. 2011 Direct numerical simulation of hypersonic turbulent boundary layers. Part 3. Effect of Mach number. *J. Fluid Mech.* **672**, 245–267.

EBADI, A., MEHDI, F. & WHITE, C. M. 2015 An exact integral method to evaluate wall heat flux in spatially developing two-dimensional wall-bounded flows. *Intl J. Heat Mass Transfer* **84**, 856–861.

FAN, Y., CHENG, C. & LI, W. 2019 Effects of the Reynolds number on the mean skin friction decomposition in turbulent channel flows. *Z. Angew. Math. Mech.* **40** (3), 331–342.

FOYSI, H., SARKAR, S. & FRIEDRICH, R. 2004 Compressibility effects and turbulence scalings in supersonic channel flow. *J. Fluid Mech.* **509**, 207–216.

FUKAGATA, K., IWAMOTO, K. & KASAGI, N. 2002 Contribution of Reynolds stress distribution to the skin friction in wall-bounded flows. *Phys. Fluids* **14** (11), L73–L76.

GAD-EL HAK, M. 1994 Interactive control of turbulent boundary layers – A futuristic overview. *AIAA J.* **32** (9), 1753–1765.

DE GIOVANETTI, M., HWANG, Y. & CHOI, H. 2016 Skin-friction generation by attached eddies in turbulent channel flow. *J. Fluid Mech.* **808**, 511–538.

GOMEZ, T., FLUTET, V. & SAGAUT, P. 2009 Contribution of Reynolds stress distribution to the skin friction in compressible turbulent channel flows. *Phys. Rev.* E **79** (3), 035301.

HUANG, P. G. & COLEMAN, G. N. 1994 Van Driest transformation and compressible wall-bounded flows. *AIAA J.* **32** (10), 2110–2113.

HUANG, P. G., COLEMAN, G. N. & BRADSHAW, P. 1995 Compressible turbulent channel flows: DNS results and modelling. *J. Fluid Mech.* **305**, 185–218.

HUTCHINS, N. & MARUSIC, I. 2007*a* Evidence of very long meandering features in the logarithmic region of turbulent boundary layers. *J. Fluid Mech.* **579**, 1–28.

HUTCHINS, N. & MARUSIC, I. 2007*b* Large-scale influences in near-wall turbulence. *Phil. Trans. R. Soc. Lond.* A **365** (1852), 647–664.

HWANG, J. & SUNG, H. J. 2017 Influence of large-scale motions on the frictional drag in a turbulent boundary layer. *J. Fluid Mech.* **829**, 751–779.

IWAMOTO, K., FUKAGATA, K., KASAGI, N. & SUZUKI, Y. 2005 Friction drag reduction achievable by near-wall turbulence manipulation at high Reynolds numbers. *Phys. Fluids* **17** (1), 011702.

JIANG, G.-S. & SHU, C.-W. 1996 Efficient implementation of weighted ENO schemes. *J. Comput. Phys.* **126** (1), 202–228.

KAMETANI, Y., FUKAGATA, K., ÖRLÜ, R. & SCHLATTER, P. 2015 Effect of uniform blowing/suction in a turbulent boundary layer at moderate Reynolds number. *Intl J. Heat Fluid Flow* **55**, 132–142.

KIM, J. S., HWANG, J., YOON, M., AHN, J. & SUNG, H. J. 2017 Influence of a large-eddy breakup device on the frictional drag in a turbulent boundary layer. *Phys. Fluids* **29** (6), 065103.

KIM, K. C. & ADRIAN, R. J. 1999 Very large-scale motion in the outer layer. *Phys. Fluids* **11** (2), 417–422.

LAADHARI, F. 2007 Reynolds number effect on the dissipation function in wall-bounded flows. *Phys. Fluids* **19** (3), 038101.

LEE, J. H. & SUNG, H. J. 2011 Very-large-scale motions in a turbulent boundary layer. *J. Fluid Mech.* **673**, 80–120.

LEE, M. & MOSER, R. D. 2015 Direct numerical simulation of turbulent channel flow up to $Re_\tau \approx 5200$. *J. Fluid Mech.* **774**, 395–415.

LOZANO-DURÁN, A. & JIMÉNEZ, J. 2014 Effect of the computational domain on direct simulations of turbulent channels up to $Re_\tau = 4200$. *Phys. Fluids* **26** (1), 011702.

MEHDI, F., JOHANSSON, T. G., WHITE, C. M. & NAUGHTON, J. W. 2014 On determining wall shear stress in spatially developing two-dimensional wall-bounded flows. *Exp. Fluids* **55** (1), 1656.

MEHDI, F. & WHITE, C. M. 2011 Integral form of the skin friction coefficient suitable for experimental data. *Exp. Fluids* **50** (1), 43–51.

MODESTI, D. & PIROZZOLI, S. 2016 Reynolds and Mach number effects in compressible turbulent channel flow. *Intl J. Heat Fluid Flow* **59**, 33–49.

MODESTI, D. & PIROZZOLI, S. 2019 Direct numerical simulation of supersonic pipe flow at moderate Reynolds number. *Intl J. Heat Fluid Flow* **76**, 100–112.

MODESTI, D., PIROZZOLI, S., ORLANDI, P. & GRASSO, F. 2018 On the role of secondary motions in turbulent square duct flow. *J. Fluid Mech.* **847**, R1.

MONTY, J. P., HUTCHINS, N., NG, H. C. H., MARUSIC, I. & CHONG, M. S. 2009 A comparison of turbulent pipe, channel and boundary layer flows. *J. Fluid Mech.* **632**, 431–442.

MORINISHI, Y., TAMANO, S. & NAKABAYASHI, K. 2004 Direct numerical simulation of compressible turbulent channel flow between adiabatic and isothermal walls. *J. Fluid Mech.* **502**, 273–308.

MORKOVIN, M. V. 1962 Effects of compressibility on turbulent flows. *Mécanique de la Turbulence* **367**, 380.

MOSER, R. D., KIM, J. & MANSOUR, N. N. 1999 Direct numerical simulation of turbulent channel flow up to $Re_\tau = 590$. *Phys. Fluids* **11** (4), 943–945.

NONOMURA, T. & FUJII, K. 2009 Effects of difference scheme type in high-order weighted compact nonlinear schemes. *J. Comput. Phys.* **228** (10), 3533–3539.

NONOMURA, T., IIZUKA, N. & FUJII, K. 2010 Freestream and vortex preservation properties of high-order weno and wcns on curvilinear grids. *Comput. Fluids* **39** (2), 197–214.

NONOMURA, T., LI, W., GOTO, Y. & FUJII, K. 2011 Improvements of efficiency in seventh-order weighted compact nonlinear scheme. *CFD J.* **18** (2), 180–186.

PATEL, A., BOERSMA, B. J. & PECNIK, R. 2016 The influence of near-wall density and viscosity gradients on turbulence in channel flows. *J. Fluid Mech.* **809**, 793–820.

PATEL, A., PEETERS, J. W., BOERSMA, B. J. & PECNIK, R. 2015 Semi-local scaling and turbulence modulation in variable property turbulent channel flows. *Phys. Fluids* **27** (9), 095101.

PECNIK, R. & PATEL, A. 2017 Scaling and modelling of turbulence in variable property channel flows. *J. Fluid Mech.* **823**, R1.

PEET, Y. & SAGAUT, P. 2009 Theoretical prediction of turbulent skin friction on geometrically complex surfaces. *Phys. Fluids* **21** (10), 105105.

RENARD, N. & DECK, S. 2016 A theoretical decomposition of mean skin friction generation into physical phenomena across the boundary layer. *J. Fluid Mech.* **790**, 339–367.

TRETTEL, A. & LARSSON, J. 2016 Mean velocity scaling for compressible wall turbulence with heat transfer. *Phys. Fluids* **28** (2), 026102.

WALZ, A. 1959 Compressible turbulent boundary layers with heat transfer and pressure gradient in flow direction. *J. Res. Natl Bur. Stand.* **63**, 53–70.

YOON, M., AHN, J., HWANG, J. & SUNG, H. J. 2016 Contribution of velocity–vorticity correlations to the frictional drag in wall-bounded turbulent flows. *Phys. Fluids* **28** (8), 081702.

ZHANG, Y.-S., BI, W.-T., HUSSAIN, F. & SHE, Z.-S. 2014 A generalized Reynolds analogy for compressible wall-bounded turbulent flows. *J. Fluid Mech.* **739**, 392–420.